高等学校化学学报
CHEMICAL JOURNAL OF CHINESE UNIVERSITIES
研究论文

碳点调控混合相钛酸钠的储钠性能

李　丹[1]，胡鸿辉[1]，侯红帅[2]，张　生[3]，刘立杰[4]，景明俊[1]，吴天景[1]
（1. 湘潭大学新能源装备及储能材料与器件国家国际科技合作基地，新型储能电池关键材料制备技术国家地方联合工程实验室，环境友好化学与应用教育部重点实验室，湘潭 411105；
2. 中南大学化学化工学院，粉末冶金国家重点实验室，长沙 410083；
3. 河南大学纳米科学与工程研究所，开封 475004；4. 河南农业大学理学院，郑州 450002）

摘要　$Na_2Ti_3O_7$和$Na_2Ti_6O_{13}$是两种典型的钛基储钠材料，分别具有理论容量高和结构稳定性好的优点，而调控两者在复合材料中的占比是更好发挥其电化学性能的关键．基于碳点比表面积大、表面官能团丰富等优势，本文利用一步水热法，原位制得了含碳点的钛酸钠前驱体．经过后续的热转换处理，可获得含由碳点衍生而来的导电碳的$Na_2Ti_3O_7$和$Na_2Ti_6O_{13}$复合材料(NNTO/C)．导电碳的引入对混合相的组分比例进行了调控，还为复合材料提供了小电荷转移阻抗(R_{ct}, 7.48 Ω)和大比表面积(100.8 m^2/g)，使得NNTO/C发挥混合相协同互补作用的同时，展现出更好的储钠行为．将其用作负极时，NNTO/C在0.05 A/g的电流密度下循环超200次，仍有143.8 mA·h/g的比容量，并在1.00 A/g的大电流下循环400次后展现出108 mA·h/g的比容量．本研究为电极材料两相结构的设计及碳点在储能方面的拓展应用给予了新思路．

关键词　$Na_2Ti_3O_7$；$Na_2Ti_6O_{13}$；混合相；碳点；储钠行为
中图分类号　O614；O646　　**文献标志码**　A　　doi：10.7503/cjcu20240356

Sodium Storage Performance of Mixed-phase Sodium Titanate Tuned by Carbon Dots

LI Dan[1], HU Honghui[1], HOU Hongshuai[2], ZHANG Sheng[3], LIU Lijie[4*], JING Mingjun[1*], WU Tianjing[1*]
(*1. National Base for International Science & Technology Cooperation, National Local Joint Engineering Laboratory for Key Materials of New Energy Storage Battery, Key Laboratory of Environmentally Friendly Chemistry and Application of Ministry of Education, Xiangtan University, Xiangtan* 411105, *China*;
2. State Key Laboratory of Powder Metallurgy, College of Chemistry and Chemical Engineering, Central South University, Changsha 410083, *China*; *3. Institute of Nanoscience and Engineering Henan University, Kaifeng* 475004, *China*; *4. College of Science Henan Agricultural University, Zhengzhou* 450002, *China*)

Abstract　$Na_2Ti_3O_7$ and $Na_2Ti_6O_{13}$ are two typical titanate-based sodium-storage materials, featuring the high

收稿日期：2024-07-16. 网络首发日期：2024-09-04.
联系人简介：吴天景，男，博士，副教授，主要从事能源材料、光电功能材料及器件方面的研究．E-mail: twu@xtu.edu.cn
景明俊，女，博士，副教授，主要从事无机材料的制备及其在储能领域应用方面的研究．E-mail: jingmingjun@xtu.edu.cn
刘立杰，男，博士，教授，主要从事有机硼光电功能材料及其机理方面的研究．E-mail: lijieliu@henau.edu.cn
基金项目：湖南省自然科学基金杰出青年基金(批准号: 2023JJ10041)、湖南省教育厅基金(批准号: 22A0114)、河南省自然科学基金(批准号: 232300421228)、河南农业大学拔尖人才计划项目(批准号: 30501032)、国家自然科学基金(批准号: 22305070)和国家大学生创新实验计划资助项目(批准号：S202310530037X)资助．
Supported by the Distinguished Young Scholar Fund Project of Hunan Province Natural Science Foundation, China(No.2023JJ10041), the Hunan Provincial Education Office Foundation of China(No.22A0114), the Natural Science Foundation of Henan Province, China(No.232300421228), the Topnotch Talents Program of Henan Agricultural University, China(No. 30501032), the National Natural Science Foundation of China (No.22305070) and the National College Students Innovative Experimental Program Funding Project, China(No.S202310530037X).

theoretical capacity and favorable structure stability, respectively. Regulating the ratio of them in the composite material is the key to strengthen its electrochemical characteristics. Herein, based on the high specific surface area and abundant surface functional groups of carbon dots (CDs), sodium titanate precursors containing CDs were *in situ* prepared by one-step hydrothermal method. After the thermal conversion of the precursors, a composite material (NNTO/C) of $Na_2Ti_3O_7$ and $Na_2Ti_6O_{13}$ was obtained, containing conductive carbon derived from CDs. The introduction of conductive carbon not only adjusts the composition ratio of the mixed phases, but also provides a small charge transfer impedance (R_{ct}, 7.48 Ω) and a big specific surface area (100.8 m^2/g). As a result, NNTO/C composites exhibit better sodium storage behavior while playing the synergistic interaction of mixed phases. When employed as the anode, after 200 cycles at 0.05 A/g, NNTO/C still maintains a specific capacity of 143.8 mA·h/g. After 400 cycles at 1.00 A/g, the specific capacity remains as high as 108 mA·h/g. This study suggests an innovative thinking for designing two-phase structures of electrode materials and the greater use of CDs in electrochemical energy storage.

Keywords $Na_2Ti_3O_7$; $Na_2Ti_6O_{13}$; Mixed-phases; Carbon dots; Sodium storage behavior

1 Introduction

Lithium-ion batteries (LIBs) universally operate in a multitude of electronic equipment after decades of prosperous development[1]. However, the constrained and unequal allocation of lithium resources has compelled researchers to find new secondary batteries to replace LIBs[2-4]. Sodium exhibits analogous physicochemical properties of lithium, and its reserve is abundant and generally distributed in the world. Hence, sodium-ion batteries (SIBs) are viewed ideal for superseding LIBs[5]. Nevertheless, Na^+ ions possess greater radius and mass than Li^+ ions, while many electrode materials commonly employed for LIBs are not suitable for SIBs[6]. With graphite applied in SIBs as an example, its insertion potential is approximately 0 V, which easily leads to the generation of sodium dendrites and its capacity is limited to 31 mA·h/g in ester-based electrolytes[7]. Thus, the selection of appropriate electrode materials represents a pivotal step in the advancement of SIBs.

Depending on the different mechanisms of Na^+ ion storage, SIBs anode materials can generally be categorized as intercalation type, conversion type, and alloy type. As a typical insertion material, titanium-based compounds have garnered extensive attention due to their exceptional attributes of high cycle stability, low voltage platform, cost-effectiveness, and so forth[8]. $Na_2Ti_3O_7$ and $Na_2Ti_6O_{13}$, as delegates, have been extensively studied in terms of energy storage. $Na_2Ti_3O_7$ is defined by a distinctive layered structure comprising zigzag TiO_6 octahedra, and each formulation unit can reversibly insert two Na^+ ions, demonstrating a considerable reversible capacity of 177 mA·h/g. Besides, the lowest mean Na intercalation potential (0.3 V) of $Na_2Ti_3O_7$ contributes to its high energy density and mitigates the formation of sodium dendrites[9]. However, the application and development of $Na_2Ti_3O_7$ are impeded by the low conductivity resulting from the wide energy gap (3.7 eV). As opposed to $Na_2Ti_3O_7$, $Na_2Ti_6O_{13}$ exhibits high ionic conductivity and good structural stability in SIBs[10,11]. This is mainly because every three co-edge TiO_6 octahedral forms a 3D frame with two different-sized tunnels in $Na_2Ti_6O_{13}$, the tunnel size is larger than Na^+ ion radius and is well suited for Na^+ ion storage[12]. Unfortunately, the low sodium storage capacity of $Na_2Ti_6O_{13}$ hinders its further application.

For the respective characteristics of the two materials, many improvement strategies have been implemented, such as extending layer spacing[13], mixed with conductive materials[10,14], and constructing novel structures[15]. Strategies for the construction of two-phase composites have also been proposed with the intention of counteracting the confines of single material and enhancing the electrochemical behavior of electrodes. Cech *et al.*[16] reported the fabrication of $Na_2Ti_3O_7$ (42%) and $Na_2Ti_6O_{13}$ (58%) nanorods by microwave-assisted hydrothermal methodology. Under the rate of C/5, the composite has better stability than the single-phase

structure, maintaining a capacity of 65 mA·h/g. Chandel *et al.* [17] used cetyltrimethyl ammonium bromide (CTAB) as a carbon source to prepare nanocomposites of $Na_2Ti_3O_7$(18%) and $Na_2Ti_6O_{13}$(82%), which have high reversible capacity (161 mA·h/g) and superb rate capability. Hwang *et al.* [18] reported $Na_2Ti_3O_7$ and $Na_2Ti_6O_{13}$ hybrids synthesized *via* using supercritical methanol and carbon dioxide coatings. At 1 A/g, the mixed material has a capacity of 44 mA·h/g. To conclude, compositing layered $Na_2Ti_3O_7$ with tunneled $Na_2Ti_6O_{13}$ is an effective strategy to ameliorate their electrochemical behaviors. More importantly, it is worth considering how to regulate the proportion of the two phases in the composite materials to achieve the ideal electrochemical performance.

Carbon dots (CDs) are a category of materials with nanoparticle size smaller than 10 nm and dominated by carbon. They are usually composed of sp^2/sp^3 carbon framework and plentiful O/H-containing functional groups or polymer chains[19,20]. By screening suitable carbon sources and synthesis conditions, the size, crystallinity, and functional groups of CDs can be regulated according to the demand[21]. When other materials are combined with CDs, conductive carbon can be introduced after high-temperature calcination. This occurs because, during high temperature pyrolysis, CDs can be formed into conductive carbon by the polymerization of surface functional groups[22]. Conductive carbon can enhance the conductivity of the material, promoting electron transport. It also maintains structural integrity by inhibiting volume expansion in the material during cycling[23]. Owing to these superiorities, CDs have been broadly harnessed in power storage devices such as supercapacitors[24], LIBs[25], SIBs[26,27], and zinc-ion batteries (ZIBs)[28].

Based on the above background, a nanocomposite material of $Na_2Ti_3O_7$ and $Na_2Ti_6O_{13}$ containing conductive carbon (NNTO/C) was obtained. The titanium source is P25 (commercial TiO_2 containing 25% rutile and 75% anatase), and the conductive carbon is derived from the CDs. The design process consists of only one step hydrothermal method and simple thermal conversion. The composition and structure of the material were analyzed using a variety of characterization methods, and the impact of derived carbon on the electrochemical behavior of the composites was explored in detail. The introduction of conductive carbon successfully regulates the composition ratio of $Na_2Ti_3O_7$ and $Na_2Ti_6O_{13}$ in the mixed phases. Meanwhile, it effectively increases the conductivity to expedite charge transfer and enlarge the specific surface area providing additional reaction activity sites for Na^+ ion storage. When the current density is 50 mA/g, as SIBs anode, NNTO/C unfolds an initial coulombic efficiency (ICE) of 62%, and keeps a specific capacity of 143.8 mA·h/g over 200 cycles. During the rate performance test, even at higher current of 2000 mA/g, NNTO/C still remains at 94 mA·h/g, and the capacity shows minimal attenuation when the current returns to its original 50 mA/g.

2 Experimental

2.1 Materials and Measurements

P25 (commercial TiO_2) was bought in Shanghai Macklin Biochemical Technology Co., Ltd. Carboxymethyl cellulose sodium (CMC, C. P. grade) was produced by The dow chemical company. Sodium (Na, A. R. grade) was purchased from Guo Yao Company. Acetylene black (C, Battery level) was from Tianjin Yiborui Chemical Co., Ltd. Sodium hydrate (NaOH, A. R. grade) was purchased in Tianjin Damao Chemical Reagent Factory. Sodium hexafluorophosphate ($NaPF_6$, battery level) and diethylene glycol dimethyl ether (DEGDME, battery level) were procured from Shanghai Songjing New Energy Technology Co., Ltd..

Scanning electron microscopy (SEM, Hitachi SU-3500, Hitachi High-Tech Corporation, Japan) was taken to detect the shape of the materials. The crystal structure and purity were defined using X-ray diffraction (XRD, Ultima IV, Rigaku Corporation, Japan) with Cu $K\alpha$ radiation (λ=0.15406 nm). Measurement of powder microstructure and phase composition was done using the transmission electron microscopy (TEM,

JEM-2100, JEOL Co. Ltd., Japan) at 200 kV accelerated voltage. Raman spectral analysis was conducted using the Invia instrument(Raman, invia, Renishaw plc, UK). The Brunauer Emmett-Teller(BET, TriStar II 3020, Micromeritics, America) was adopted to ascertained the nitrogen adsorption-desorption isotherms. The ESCALAB Xi+(America) device was utilized to acquire data for X-ray photoelectron spectroscopy(XPS). Under air conditions, the carbon content of NNTO/C composite was determined using thermogravimetric analysis(TGA 50, TA Instruments, America).

2.2 Material Preparation

2.2.1 Preparation of Carbon Dots The synthesis of CDs was based on our earlier report[29].

2.2.2 Preparation of NNTO Firstly, the dispersion of 0.2 g P25 in 40 mL 10 mol/L NaOH solution was achieved by stirring at room temperature for 15 min, followed by ultrasound to make dispersion more uniform. The resulting suspension was placed in a Teflon-lined autoclave(100 mL) and reacted at 120 ℃ for 24 h. After the reaction was complete, the produce was washed to neutral with pure water, and then dried at 60 ℃ to get the precursors. In the argon atmosphere, the precursors were calcined at 600 ℃ for 2 h with a heating rate of 5 ℃/min to acquire the end white product.

2.2.3 Preparation of NNTO/C 0.2 g P25 and a certain mass(0.15 g) of CDs were stirred with 40 mL 10 mol/L NaOH aqueous for 15 min at room temperature, and then sonicated; the remaining steps were consistent with the preparation of NNTO. After calcination was completed, a black product was obtained.

2.2.4 Electrochemical Performance Measurements To test electrochemical properties, the active material, acetylene black, and CMC at a mass ratio of 7∶1.5∶1.5 were stirred evenly in pure water. Next, the slurry was applied to copper foil and dried for an entire night at 60 ℃ under vacuum conditions. The assembly of CR 2016 button-type batteries was conducted in an Ar-filled glove box that contains less than 10^{-8} of oxygen and water. Glass fiber was used as separator, metal sodium sheet was used as counter electrode of the half battery, and 1.0 mol/L $NaPF_6$ in DEGDME was used as electrolyte. The NEWARE test system was used for galvanostatic charge-discharge(GCD) examination, with a voltage of 0.01—2.50 V. Electrochemical impedance spectroscopy(EIS) test frequency was in the range of 0.01—100 kHz. EIS and cyclic voltammetry(CV) were undertaken at CHI660E electrochemical test station.

3 Results and Discussions

3.1 Compositions and Morphologies

Scheme 1 presents the synthesis diagram of NNTO/C nanocomposites, which mainly involves one-step hydrothermal process and calcination treatment. Firstly, the yellow precursor containing CDs was prepared *in situ* by one-step hydrothermal method. After thermal conversion of the precursor under argon, the final black product(NNTO/C) was obtained. At the same condition, a mixed phase(NNTO) of $Na_2Ti_3O_7$ and $Na_2Ti_6O_{13}$ was prepared as a blank without CDs. Pictures of the precursor and final product of NNTO are shown in Fig.S1(see the Supporting Information of this paper).

The morphology of the two materials and the microstructure of NNTO/C are detailed in Fig. 1. From

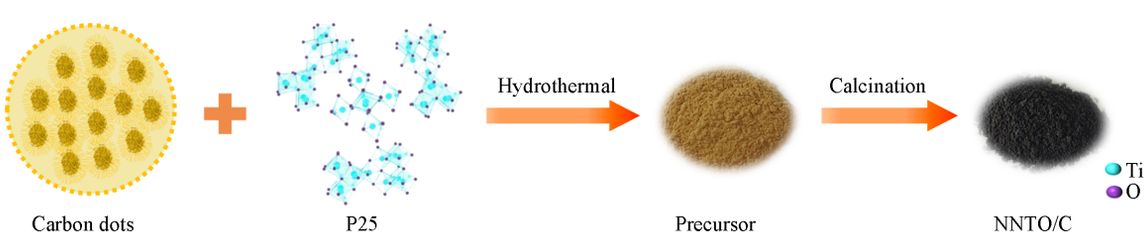

Scheme 1 Schematic diagram of NNTO/C preparation process

Fig.1(A) and (B), it can be observed that both NNTO and NNTO/C are composed of homogeneous nanoparticles with dispersive aggregation characteristics. The morphology of NNTO/C is slightly different from that of pure NNTO, and the introduction of CDs curbs the agglomeration of nanoparticles to a certain extent. A reduction in the diffusion path length for electron/ion transport is facilitated by the nanoparticles. TEM images further reveal the microstructure of NNTO/C. The existence of numerous nanoparticles can be detected in Fig. 1(C), but the presence of $Na_2Ti_3O_7$, $Na_2Ti_6O_{13}$, and carbon matrix derived from CDs cannot yet be determined. The high-resolution transmission (HRTEM) picture displayed in Fig. 1(D), however, provides confirmation of the presence of two phases and carbon matrix. HRTEM images reveal distinct lattice fringes in $Na_2Ti_3O_7/Na_2Ti_6O_{13}/C$. The measured *d*-spacing of 0.687 and 0.757 nm corresponds to the $(\bar{1}01)$ face of $Na_2Ti_3O_7$ and the (200) face of $Na_2Ti_6O_{13}$, respectively. This indicates the presence of both $Na_2Ti_3O_7$ and $Na_2Ti_6O_{13}$ in nanoparticles[12,30]. Furthermore, Fig.1(D) expressly shows the characteristics of the amorphous carbon, marked with red lines, proving that the carbon matrix derived from the CDs is equally present in the nanoparticles. The carbon matrix will be helpful in enhancing electrochemical utilization and alleviating the volume expansion of the material.

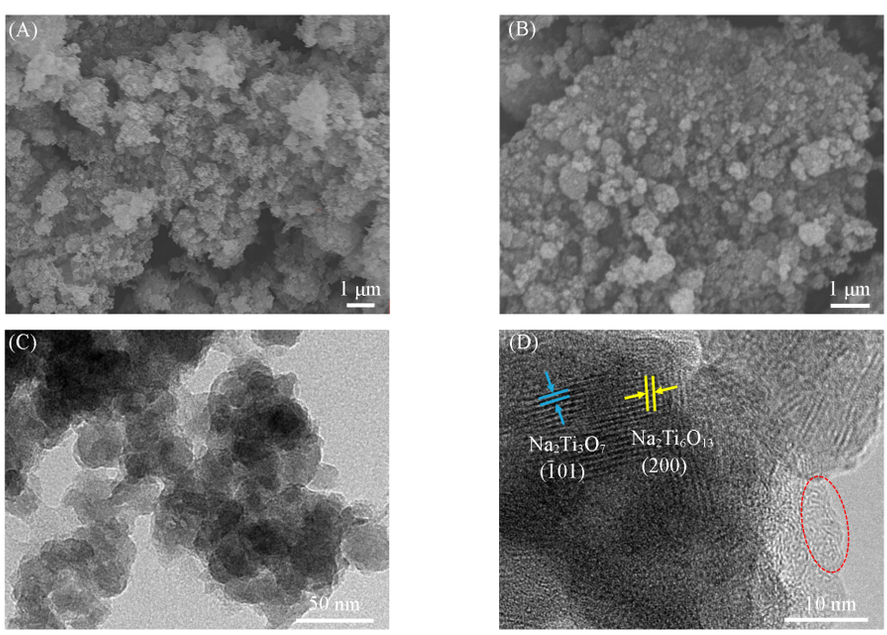

Fig. 1 SEM images of NNTO(A) and NNTO/C(B), TEM(C) and HRTEM images(D) of NNTO/C

The structures and phase composition of NNTO and NNTO/C were investigated using XRD. Fig.S2(A) (see the Supporting Information of this paper) depicts the XRD patterns of the precursors of the two materials (washed to neutral after hydrothermal completion and then dried at 60 ℃). The main peak at 2θ=9.6° is the signature peak of layered sodium titanates. The precursor of the material with CDs has a clearer broad peak at about 20° compared with the blank sample, which can be attributed to the characteristic diffraction peak of carbon. The chemical formula for the precursor of pure NNTO may be $Na_xH_{2-x}Ti_3O_7 \cdot nH_2O$ ($0<x<2$, $n<1$), as confirmed by XRD patterns and previous reports[31]. As displayed in Fig.2(A), after calcination at 600 ℃, the compositions of NNTO and NNTO/C were examined by XRD. The crystal structure of the material undergoes changes due to the removal of interlayer water, leading to corresponding alterations in the XRD pattern, and shows a combination of $Na_2Ti_3O_7$ and $Na_2Ti_6O_{13}$ phase. The characteristic peaks of $Na_2Ti_3O_7$ and $Na_2Ti_6O_{13}$ can be discovered in the diffraction peaks of both materials, and after introducing conductive carbon, there is no other diffraction peaks showed up. This means that NNTO and NNTO/C composites have been successfully

synthesized. In NNTO/C, carbon derived from CDs exists in an amorphous structure. The diffraction peak of NNTO/C is weaker than that of NNTO. This may be due to the bonding between NNTO and the carbon matrix.

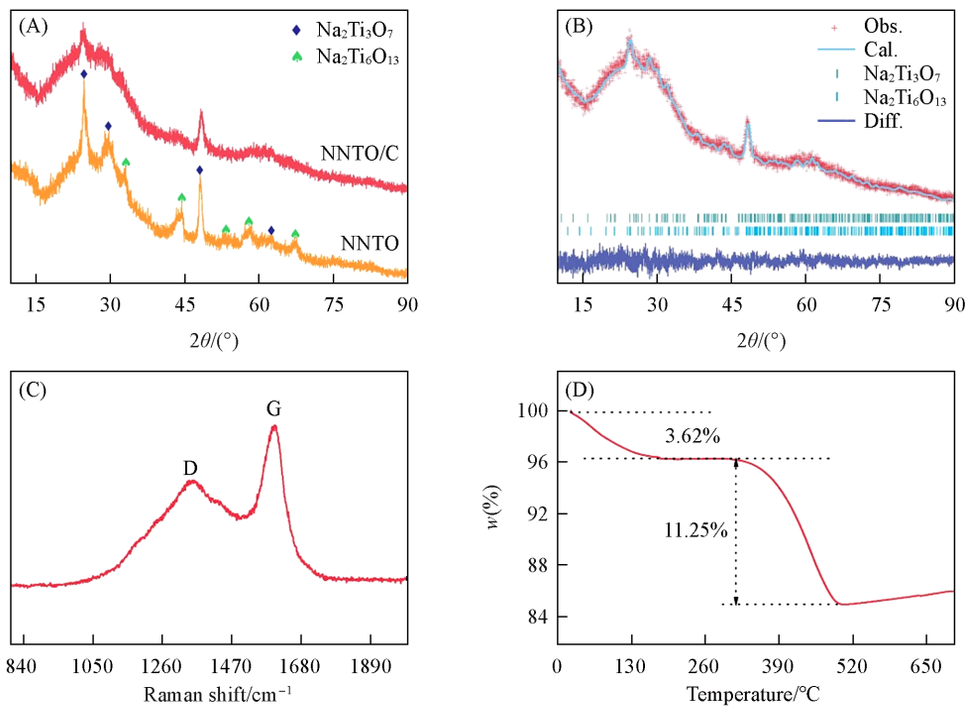

Fig. 2 XRD patterns of NNTO and NNTO/C composites(A), Rietveld refinement(B), Raman analysis(C) and TGA profiles(D) of NNTO/C sample

Later, in order to research the relative composition of $Na_2Ti_3O_7$ and $Na_2Ti_6O_{13}$ in the NNTO/C composite, Fig.2(B) exhibits the Rietveld refinement XRD pattern of NNTO/C. According to the results, the contents of $Na_2Ti_3O_7$ and $Na_2Ti_6O_{13}$ are 34% and 66%, respectively, after carbon content is removed. Similarly, as illustrated in Fig.S2(B), the contents of $Na_2Ti_3O_7$ and $Na_2Ti_6O_{13}$ in NNTO are 35.9% and 64.1%, respectively. The differing relative contents of the two phases in NNTO and NNTO/C suggest that the addition of CDs effectively regulates the composites. The $Na_2Ti_6O_{13}$ phase is the dominant phase in NNTO/C, which helps the electrode material to exhibit better cycling performance. In addition, the higher $Na_2Ti_3O_7$ ratio than previously reported, resulting in higher reversible capacity in NNTO/C[11].

To understand the existence form of carbon in NNTO/C nanocomposites, Raman test on NNTO/C was carried out. It can be clear from Fig.2(C) that the G and D bands are situated in 1582 and 1335 cm^{-1}, indicating the successful introduction of CDs. As is well known, the D and G band are associated with the sp^3 carbon and sp^2 graphite structure, respectively. Here, the D and G bands share an approximate intensity ratio of 0.69. This confirms that the carbon exhibits a relatively high graphitic feature, which can lead to an increase in conductivity. The carbon content of NNTO/C was determined through a TGA test, with the result depicted in Fig.2(D). At the test temperature, there are two significant weight loss periods as shown by the TGA curves. Upon reaching a temperature of 181 ℃, the weight is reduced by 3.62% with the elimination of adsorbed water. The reduction in weight observed at approximately 313—500 ℃ can be attributed to the combustion of carbon. It is calculated that the carbon content of NNTO/C is 11.25%.

The N_2 adsorption-desorption curves were studied to fully comprehend the impact of CDs on the specific surface area or porosity of the samples. As evidenced in Fig.3(A), NNTO/C has the IV-type adsorption/desorption isotherm with H3 hysteresis loop, which is unique to mesoporous materials[32]. At approximately 3.19 and 5.85 nm, the corresponding pore distribution exhibits two noticeable peaks, and almost all the

pores are below 6.5 nm, providing further evidence for the presence of mesoporous structures. The mesoporous structure facilitates the transport of ions within the electrode. The N_2 adsorption-desorption isotherm and pore size distribution of NNTO were illustrated in Fig.3(B). On account of Bruner-Emmet-Teller(BET) equation, NNTO/C composites are equipped with a specific surface area of 100.8 m^2/g, higher than 70.6 m^2/g of NNTO. The active site of electrochemical reaction is increased and electrode contact with electrolyte is facilitated by its larger surface area. However, according to Barrett Joyner-Halenda(BJH) model, the average pore width of NNTO/C(8.96 nm) is smaller than that of NNTO(30.78 nm), and NNTO may have a faster kinetic pseudo-capacitance reaction than NNTO/C.

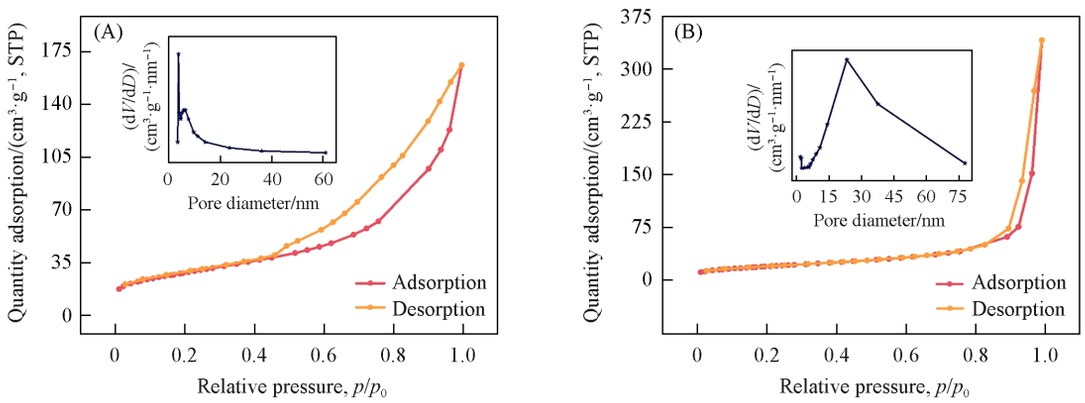

Fig. 3 N_2 adsorption-desorption isotherms and pore size distributions(insets) of NNTO/C(A) and NNTO(B)

The composition and the surface chemical bonding states of NNTO/C were further analyzed with XPS. Na, Ti, and O are present in the product, as confirmed by the XPS survey spectrum of NNTO/C, displayed in Fig.4(A) and Table S1(see the Electronic Supplementary Material of this paper). Furthermore, C element in NNTO/C composite is also observed, which is derived from CDs. Fig.4(B)—(D) illustrates the high-resolution XPS spectra of Ti_{2p}, O_{1s}, and C_{1s}, respectively. As indicated by Fig. 4(B), the $Ti_{2p_{3/2}}$ peaks are found to be at 459.18 and 458.65 eV, while the $Ti_{2p_{1/2}}$ peaks are detected at 464.9 and 464 eV. The values are in

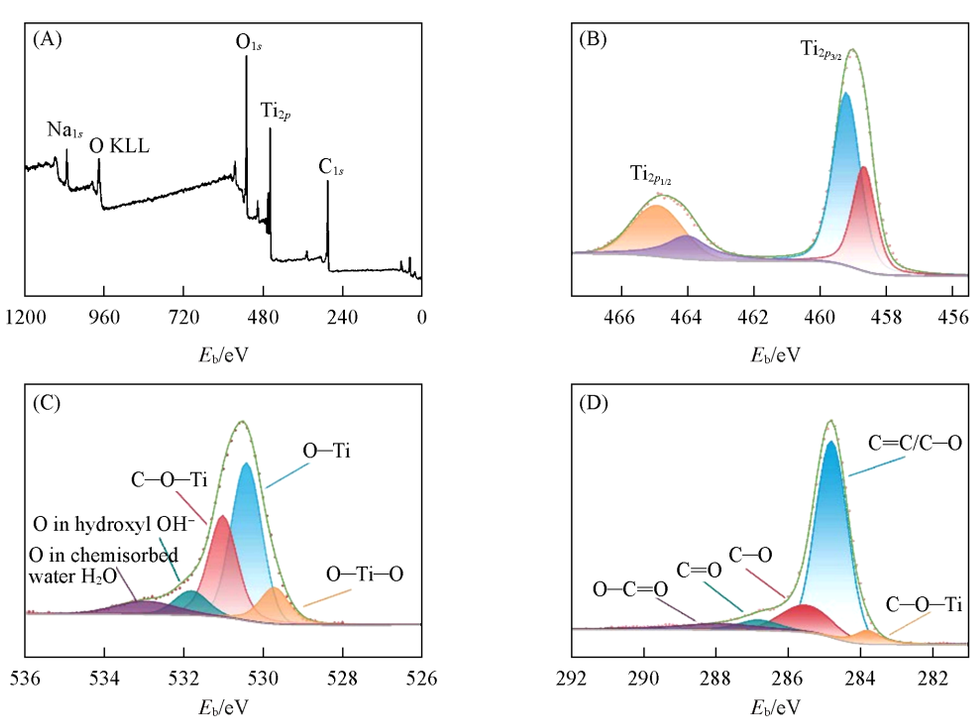

Fig. 4 XPS survey(A) and high resolution spectra for Ti_{2p}(B), O_{1s}(C) and C_{1s}(D) of NNTO/C

accordance with the $Ti_{2p3/2}$ and $Ti_{2p1/2}$ peaks in $Na_2Ti_6O_{13}$ and $Na_2Ti_3O_7$, respectively. This indicates that Ti predominantly exists in the form of Ti^{4+}. Five peaks at 529.7, 530.4, 531.0, 531.8 and 533.0 eV are found in the O_{1s} spectra. These peaks are connected to O in O—Ti—O, O—Ti, C—O—Ti, hydroxyl OH^-, as well as oxygen in chemisorbed water, respectively. Also, Fig.4(D) shows the deconvoluted C_{1s} spectra in NNTO/C. Five peaks at 283.8, 284.8, 285.5, 286.8 and 287.9 eV correspond to C—O—Ti, C=C/C—C, C=O, O—C=O, and O—C=O, respectively, confirming that NNTO/C composite is successfully synthesized.

3.2 Electrochemical Performance

The button-type half cells were assembled to research the storage properties and mechanism of Na^+ ions in NNTO/C. In the composition of the half cells, Na serves as the counter electrode, and the working electrode comprises NNTO or NNTO/C. The electrochemical characteristics of the samples was assessed *via* CV. Fig.5(A) and Fig.S3(see the Supporting Information of this paper) depict the initial three cycle CV plots of NNTO/C and NNTO when the sweep speed is 0.1 mV/s, respectively. The plots of both materials have similar characteristics, demonstrating the typical sodium storage properties of sodium titanate and high-voltage energy storage within the range from 0.5—2.5 V[33]. A wide reduction peak occurs at around 0.80 V during the initial cycle of Fig.5(A), which is linked to electrolyte decomposition and the formation of solid electrolyte interface(SEI) layer. This peak diminishes in subsequent cycles due to the irreversible reactions. At about 0.88 V, there emerges a broad cathode peak in the second and third cycles, along with a pair of faint anode peaks at 0.40 and 0.90 V. These peaks are connected to the process of Na^+ de/interaction, corresponding to the redox reactions of Ti^{4+}/Ti^{3+}[11]. Simultaneously, except for the first cycle, the CV curve is nearly identical. This indicates that NNTO/C electrode exhibits exceptional reversibility and structural stability for the insertion/extraction of Na^+ ions. Fig.5(B) gives the cycling ability of the two electrodes at 0.05 A/g. After two hundred cycles of continuous charge and discharge, there is almost no capacity decay in both NNTO and NNTO/C, and the NNTO/C displays a better stability. This shows that NNTO/C nanocomposites exhibit good reaction kinetics and excellent cycling properties due to the presence of carbon matrix derived by CDs. Within the voltage window of 0.01—2.50 V, Fig.S4(see the Supporting Information of this paper) shows the GCD curves for the 1st, 10th, 50th and 100th cycles of NNTO/C at 0.05 A/g. The first discharge capacity of NNTO/C is 254.7 mA·h/g and the initial Coulomb efficiency is 62%. This is because the electrolyte decomposition and formation of SEI film cause a large loss of specific capacity. In the discharge profile of the first cycle, a minor plateau emerges at 0.8 V and disappears in later cycles. During the subsequent charge-discharge process, the curve does not change significantly, indicating a highly reversible electrode reaction process following the initial cycle. And these findings are in harmony with CV test results. The rate performance of NNTO/C and NNTO was assessed at various current densities, as demonstrated in Fig.5(C) and(D). The capacities of NNTO/C are 149.2, 139.3, 129.4, 116.0, 104.7, and 94.5 mA·h/g at current densities of 0.05, 0.10, 0.20, 0.50, 1.00, and 2.00 A/g, respectively. Upon returning to 0.05 A/g, the NNTO/C is still exhibiting a reversible capacity of 145 mA·h/g. Under the uniform current density test conditions for NNTO/C, the specific capacities corresponding to NNTO are 115.8, 113.8, 108.6, 101.5, 95.6, and 88.9 mA·h/g, respectively. At all current densities, it can be seen that the NNTO/C electrode has a higher capacity compared to the NNTO. Fig.5(E) displays the cyclic stability of NNTO/C at a high current of 1.00 A/g, after the galvanostatic intermittent titration technique(GITT) test. After 400 cycles, NNTO/C still has a capacity of 108 mA·h/g with almost no capacity degradation, and achieves a coulombic efficiency closed to 100%.

To further explore the dynamic characteristics of sodium storage, CV curves with diverse sweep rates were tested within the range of 0.1—1.5 mV/s. In Fig.6(A), CV curves of NNTO/C at varying scanning rates

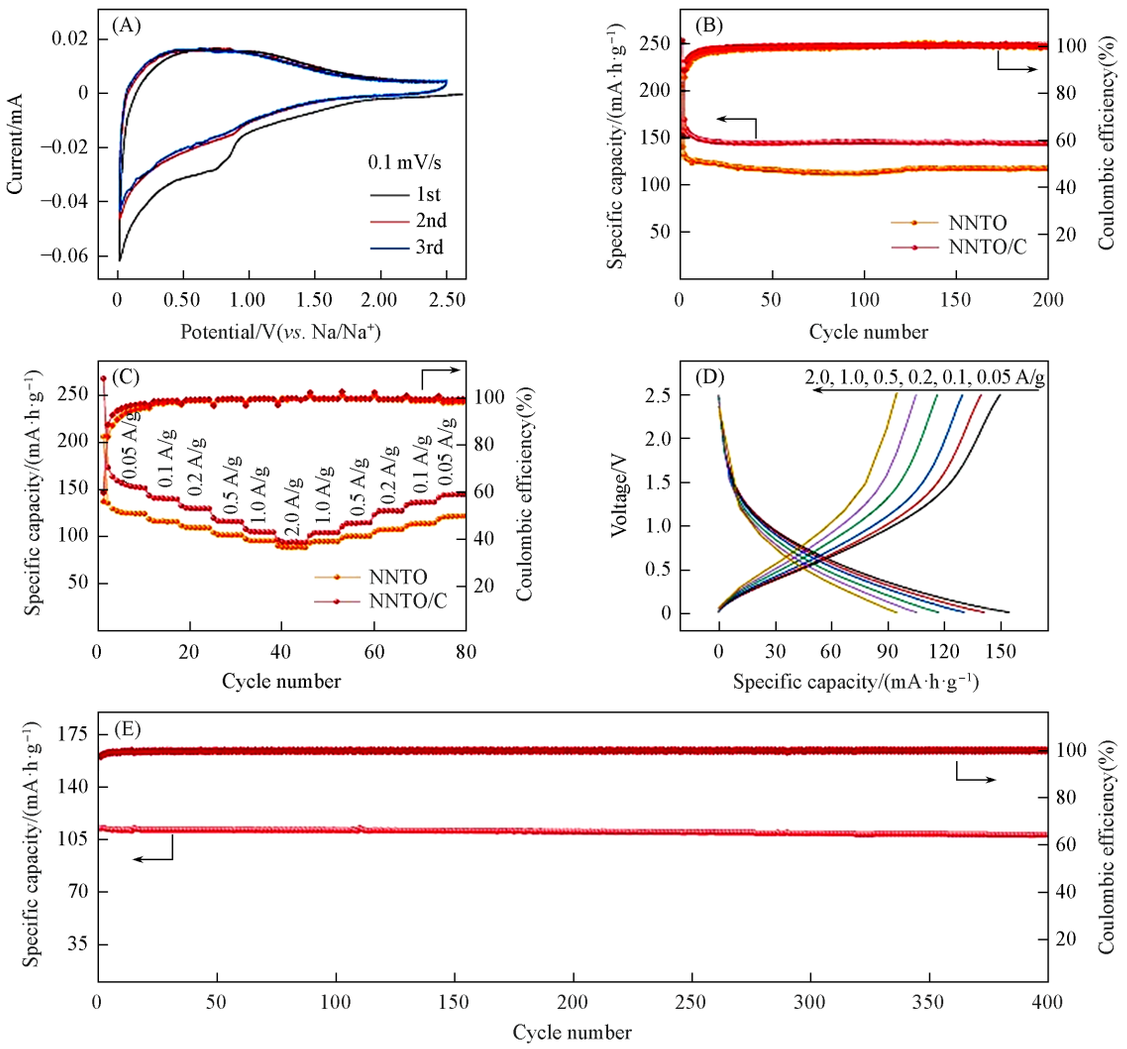

Fig. 5 CV plots of NNTO/C at 0. 1 mV/s(A), cycling performances of NNTO/C and NNTO at 0. 05 A/g(B), rate capabilities of NNTO/C and NNTO(C), charge - discharge curves of NNTO/C(D), cycling properties of NNTO/C at 1. 00 A/g(E)

have similar shapes, containing both broad cathodic and anodic peaks. As the scanning rate increases, the cathode peaks move towards the negative direction, while the anode peaks move towards the positive direction as a result of the electrode polarization process. Similarly, CV curves of NNTO have the analogous characteristics at different sweep speeds, as presented in Fig.S5(A)(see the Supporting Information of this paper). Using CV curves obtained at various sweep speeds to analyze the link between peak current(i) and scanning rate(v) can provide insight into the charge storage mechanism of NNTO and NNTO/C. According to the formula: $i=av^b$, where a and b are constant coefficients. Whether the insertion/deinsertion of Na^+ in the electrode reaction is diffusion behavior or pseudo-capacitance behavior can be judged by the b value. A value of b close to 1 means that the reaction is managed by a pseudo-capacitance process with fast dynamics. The diffusion control process assumes dominance when the b value nears 0. 5. Fig.S6(see the Supporting Information of this paper) displays the log plot of peak current *versus* sweep speed for NNTO/C and NNTO. Between 0. 1 and 1. 5 mV/s, the calculated b values of the reduction peak and oxidation peak of NNTO/C are 0. 860, 0. 896 and 0. 976, and the b values corresponding to NNTO are 0. 893, 1. 026, and 1. 028, indicating a capacitance-led electrochemical process. A large b value manifests that most of the sodium storage occur at or near the surface, and a higher b value for NNTO than NNTO/C may be related to its larger pore size. According to the

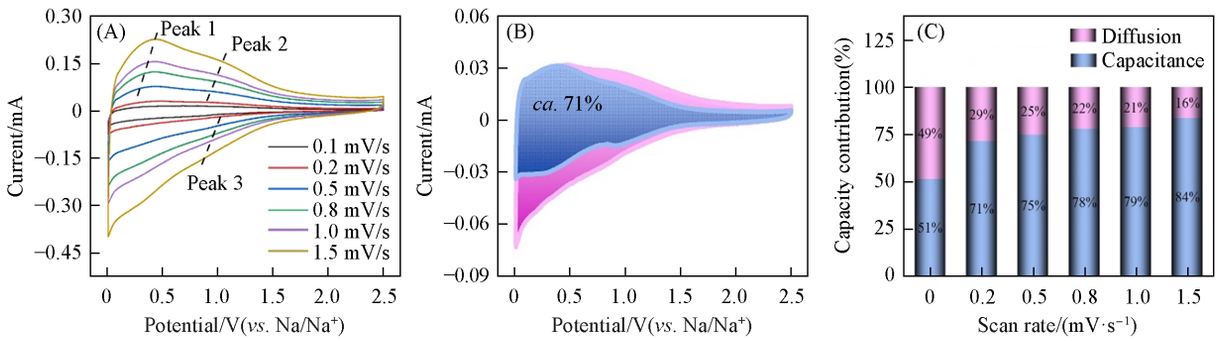

Fig. 6 CV plots at various sweep speeds(A), capacitive and diffusive contributions at 0. 2 mV/s(B), diffusion and pseudo-capacitive contributions at various scan rates of NNTO/C(C)

equation: $i(v)=k_1v + k_2v^{1/2}$, the relationship between scanning speed and current response is further quantified, and the contribution of pseudo-capacitance and diffusion control at a certain voltage is distinguished. Where i and v are variable parameters, $i(v)$ means the sum of current response at a specified potential, and k_1v as well as $k_2v^{1/2}$ typify the capacitance and diffusion contributions, respectively. At 0. 2 mV/s, the contribution rate of capacitance in total capacity is depicted in Fig.6(B) and Fig.S5(B). From the area calculation of CV curve, it can be seen that the contribution of pseudo-capacitance to capacity of NNTO/C anode at 0. 2 mV/s is 71% and NNTO is 73% at the same sweep speed. The respective ratios of pseudo-capacitance contribution and diffusion contribution of the two materials at varied scanning rates are displayed in Fig. 6(C) and Fig.S5(C). As the scanning rate is increased, the contribution rate of capacitance also rises. The contribution rate of capacitance in NNTO/C is 51%, 71%, 75%, 78%, 79%, and 84%, respectively, in accordance with the varying scanning speeds. The capacitance contribution of NNTO is about 66%, 73%, 76%, 81%, 83%, and 90%. The faster scanning speed makes the contribution of pseudo-capacity higher. The rationale for this phenomenon is that as the scanning rate increases, the diffusion time is reduced, resulting in shorter diffusion distances and smaller diffusion components. Nevertheless, the pseudo-current is kinetically variable, so the increased sweep rate does not exert a substantial impact on pseudo- capacity. The dominant pseudo-capacitance control results in efficient electrochemical behavior.

To ascertain the cause behind the observed enhancement of the electrochemical properties, the associated Nyquist plot was analyzed by fitting the equivalent circuit in Fig. 7(A). The equivalent circuit model for understanding the impedance spectrum is inset, where the resistance (R_s) is the ohmic contact impedance, and R_{ct} is the resistance at the tablet interface. The slashes in the low frequency region correspond to Warburg impedance (Z_w), connecting to the diffusion of Na^+ within the electrode material. For NNTO/C, its semicircle diameter at high frequencies is smaller than that of NNTO. The fitting values of R_s and R_{ct} are shown in

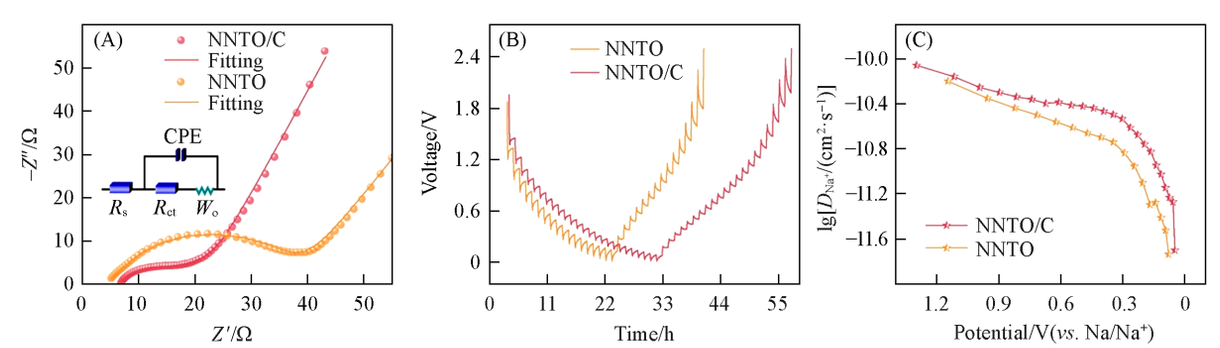

Fig. 7 Nyquist plots(A), GITT profiles(B) and Na^+ diffusion coefficient(C) of NNTO/C and NNTO

Inset of(A): equivalent circuit diagram.

Table S2 (see the Electronic Supplementary Material of this paper). The NNTO/C electrode has a lower R_{ct} value (7.48 Ω) than the NNTO electrode, indicating its conductivity can be greatly improved. The small R_{ct} value of NNTO/C is mainly attributed to synergism between different substances. Among them, conductive carbon is beneficial to improve the conductivity of NNTO/C, thus achieving excellent electrochemical properties[34]. The diffusion coefficient is obtained on the basis of the following equation[35]:

$$D_{Na^+} = \frac{4}{\pi}\frac{l^2}{\tau}\left(\frac{\Delta E_s}{\Delta E_\tau}\right)^2$$

where D_{Na^+} (cm^2/s) is the Na^+ diffusion coefficient; τ (s) is the plus time; l (cm) denotes the electrode thickness, ΔE_s (V) is the difference in voltage during charging/discharging and ΔE_τ (V) represents the voltage difference from the resting state to the equilibrium state. Fig.7(B) shows the GITT profiles of NNTO/C and NNTO at a pulse current of 0.05 A/g for 10 min, with a rest interval of 1 h. Fig.7(C) demonstrates the D_{Na^+} of NNTO/C and NNTO. By calculation, the specific value of D_{Na^+} of NNTO/C is 4.084×10^{-11} cm^2/s, greater than that of NNTO (2.951×10^{-11} cm^2/s), implying that the introduction of conductive carbon increases the reaction kinetics. The results are consistent with EIS analysis.

4 Conclusions

In conclusion, $Na_2Ti_3O_7/Na_2Ti_6O_{13}$/C (NNTO/C) nanocomposites were prepared through adding CDs *in situ*, *via* one-step hydrothermal method and heat conversion treatment. The hybrid phases were created to combine the advantages of various structures and overcome the flaws of a single phase. The carbon matrix derived from CDs not only enriches the specific surface area, but also reduces the charge transfer impedance of NNTO/C, thereby facilitating an increase in the number of active sites for Na^+ ion insertion/deinsertion and enhancing the conductivity of electrode. Furthermore, CDs effectively regulate the ratio of $Na_2Ti_3O_7$ and $Na_2Ti_6O_{13}$ in the complex, which results in superior cycling stability for the electrode material. When used as SIB anode, the prepared nanocomposites show excellent electrochemical performance in Na^+ storage. NNTO/C nanocomposites have high specific capacitance (143.8 mA·h/g after 200 cycles at a current density of 0.05 A/g) and excellent rate property (94.5 mA·h/g even at 2.0 A/g). At a high current of 1.00 A/g, the capacity remains at 108 mA·h/g even after 400 cycles, indicating high stability of the electrode structure. This work proves that the carbon matrix derived from CDs can improve the electrochemical properties of sodium titanate when used as a negative electrode material. In addition, our findings establish that two-phase structures and carbon-based composites can serve as viable electrode materials for next-generation SIBs and other power storage devices.

The Supporting Information of this paper see http://www.cjcu.jlu.edu.cn/CN/10.7503/cjcu20240356.

参 考 文 献

[1] Zhu Z. X., Jiang T. L., Ali M., Meng Y. H., Jin Y., Cui Y., Chen W., *Chem. Rev.*, **2022**, *122*(22), 16610—16751
[2] Wu N. T., Zhao Z. B., Hua R., Wang X. T., Zhang Y. M., Li J., Liu G. L., Guo D. L., Sun G., Liu X. M., Zhang J. W., *Adv. Energy Mater.*, **2024**, 2400371
[3] Zhu Y. R., Zhong W. P., Chen W. H., Hu Z. L., Xie Y. J., Deng W. T., Hou H. S., Zou G. Q., Ji X. B., *Nano Energy*, **2024**, *125*, 109524
[4] Zhu Z. X., Zhang X., Wang M. M., Chen W., *Chem. J. Chinese Universities*, **2021**, *42*(5), 1610—1618 (朱正新, 张翔, 王明明, 陈维. 高等学校化学学报, **2021**, *42*(5), 1610—1618)
[5] Zhang J. Y., Yan Y. L., Wang X., Cui Y. Y., Zhang Z. F., Wang S., Xie Z. K., Yan P. F., Chen W. H., *Nat. Commun.*, **2023**, *14*(1), 3701
[6] Jiang Y. M., Zhang Z., Liao H. Y., Zheng Y. F., Fu X. T., Lu J. N., Cheng S. Y., Gao Y. H., *ACS Nano*, **2024**, *18*(11), 7796—7824
[7] Wang J. L., Hu J. Y., Kang F. Y., Zhai D. Y., *Energy Environ. Sci.*, **2024**, *17*(9), 3202—3209

[8] Dong S. Y., Lv N., Wu Y. L., Zhang Y. Z., Zhu G. Y., Dong X. C., *Nano Today*, **2022**, *42*, 101349
[9] Dong J., Jiang Y. L., Wang R. X., Wei Q. L., An Q. Y., Zhang X. X., *J. Energy Chem.*, **2024**, *88*, 446—460
[10] Lai Q. S., Mu J. J., Liu Z. M., Zhao L. K., Gao X. W., Yang D. R., Chen H., Luo W. B., *Batteries & Supercaps*, **2023**, *6*(4), e202200549
[11] Wu C. J., Hua W. B., Zhang Z., Zhong B. H., Yang Z. G., Feng G. L., Xiang W., Wu Z. G., Guo X. D., *Adv. Sci.*, **2018**, *5*(9), 1800519
[12] Cao K. Z., Jiao L. F., Pang W. K., Liu H. Q., Zhou T. F., Guo Z. P., Wang Y. J., Yuan H. T., *Small*, **2016**, *12*(22), 2991—2997
[13] Que L. F., Yu F. D., Zheng L. L., Wang Z. B., Gu D. M., *Nano Energy*, **2018**, *45*, 337—345
[14] Zhao R., Liu C., Zhu Y. R., Zou G. Q., Hou H. S., Ji X. B., *Adv. Funct. Mater.*, **2024**, 231664
[15] Mei J., Wang T. T., Qi D. C., Liu J. J., Liao T., Yamauchi Y. K., Sun Z. Q., *ACS Nano*, **2021**, *15*(8), 13604—13615
[16] Cech O., Vaný sek P., Chladil L., Castkova K., *ECS Transactions*, **2016**, *74*(1), 331—337
[17] Chandel S., Lee S., Lee S., Kim S. J., Singh S. P., Kim J., Rai A. K., *J. Electroanal. Chem.*, **2020**, *877*, 114747
[18] Hwang J., Setiadi Cahyadi H., Chang W.Y., Kim J., *J. Supercrit. Fluid*, **2019**, *148*, 116—129
[19] Mintz K. J., Bartoli M., Rovere M., Zhou Y. Q., Hettiarachchi S. D., Paudyal S., Chen J. Y., Domena J. B., Liyanage P. Y., Sampson R., Khadka D., Pandey R. R., Huang S. X., Chusuei C. C., Tagliaferro A., Leblanc R. M., *Carbon*, **2021**, *173*, 433—447
[20] Zhai Y. P., Zhang B. W., Shi R., Zhang S. Y., Liu Y. A., Wang B. Y., Zhang K., Waterhouse G. I. N., Zhang T. R., Lu S. Y., *Adv. Energy Mater.*, **2021**, *12*(6), 2103426
[21] El-Azazy M., Osman A. I., Nasr M., Ibrahim Y., Al-Hashimi N., Al-Saad K., Al-Ghouti M. A., Shibl M. F., Al-Muhtaseb A. A. H., Rooney D. W., El-Shafie A. S., *Coord. Chem. Rev.*, **2024**, *517*, 215976
[22] Song H. Q., Wu M., Tang Z. Y., Tse J. S., Yang B., Lu S. Y., *Angew. Chem. Int. Ed.*, **2021**, *60*(13), 7234—7244
[23] Yun X. R., Li J. Y., Chen X. H., Chen H., Xiao L., Xiang K. X., Chen W. H., Liao H. Y., Zhu Y. R., *ACS Appl. Mater. Interfaces*, **2019**, *11*(40), 36970—36984
[24] Jin Y. L., Wang Y. L., Ren P. G., Zhang B. F., Zhao Z. R., Hou X., Ren F., Chen Z. Y., Guo Z. Z., Yang H. J., Li X. F., *J. Energy Storage*, **2024**, *85*, 111118
[25] Lee H. R., Kim Y. S., Lee S. Y., Son U. H., Lee S., Joh H. I., *Appl. Surf. Sci.*, **2024**, *664*, 160228
[26] Liu Z., Zhang S., Qiu Z. P., Huangfu C., Wang L., Wei T., Fan Z. J., *Small*, **2020**, *16*(38), 2003557
[27] Wu M. H., Gao Y. P., Hu Y., Zhao B., Zhang H. J., *Chin. Chem. Lett.*, **2020**, *31*(3), 897—902
[28] Liu F., Xu S. H., Gong W. B., Zhao K. T., Wang Z. M., Luo J., Li C. S., Xue P., Wang C. L., Wei L., Li Q. W., Zhang Q. C., *ACS Nano*, **2023**, *17*, 18494—18506
[29] Li L., Li Y. T., Ye Y., Guo R. T., Wang A. N., Zou G. Q., Hou H. S., Ji X. B., *ACS Nano*, **2021**, *15*, 6872—6885
[30] Zhong W., Tao M. L., Tang W. W., Gao W., Yang T. T., Zhang Y. Q., Zhan R. M., Bao S. J., Xu M. W., *Chem. Eng. J.*, **2019**, *378*, 122209
[31] Yin J., Qi L., Wang H. Y., *ACS Appl. Mater. Interfaces*, **2012**, *4*, 2762—2768
[32] Li P. X., Guo X., Zang R., Wang S. J., Zuo Y. Q., Man Z. M., Li P., Liu S. S., Wang G. X., *Chem. Eng. J.*, **2021**, *418*, 129501
[33] Wang N., Xu X., Liao T., Du Y., Bai Z. C., Dou S. X., *Adv. Mater.*, **2018**, *30*(49), 1804157
[34] Pradeep A., Kumar B. S., Verma V., Kobi S., Nandakumar T., Mukhopadhyay A., *Carbon*, **2023**, *201*, 1—11
[35] Shan H., Qin J., Ding Y. C., Sari H. M. K., Song X. X., Liu W., Hao Y. C., Wang J. J., Xie C., Zhang J. J., Li X. F., *Adv. Mater.*, **2021**, *33*(37), 2102471

(Ed.: V, K, S)